Nanowire and nanobelt arrays of zinc oxide from synthesis to properties and to novel devices†

Xudong Wang, Jinhui Song and Zhong Lin Wang*

Received 20th November 2006, Accepted 3rd January 2007
First published as an Advance Article on the web 19th January 2007
DOI: 10.1039/b616963p

This review focuses on the growth, properties and novel applications of aligned arrays of ZnO nanowires (NWs) and nanobelts (NBs) for nanogenerators and nano-piezotronics. Owing to the semiconducting and piezoelectric dual properties of ZnO crystals, novel applications are introduced using aligned ZnO NWs, such as nanogenerators. These unique properties and applications will have profound impacts in many areas, such as self-powered nanodevices and nanosystems for *in situ*, real-time and implantable biosensing and biodetection, self-powering for defence and commercial applications, and remote sensing for space technology. The article provides detailed illustrations about the synthesis method, mechanical, electrical and optical properties, as well as the underlying mechanism for piezoelectronic devices and systems.

Nanostructured materials have received broad attention due to their distinguished performance in electronics, optics and photonics.[1] With reduction in size, novel electrical, mechanical, chemical and optical properties are introduced, which are largely believed to be the result of surface and quantum confinement effects. Wire-like nanostructures are ideal systems for studying the transport process in one-dimensionally (1D) confined objects,[2] which are of benefit not only for understanding the fundamental phenomena in low-dimensional systems, but also for developing new generation nanodevices with high performance.[3] ZnO is a key technological material.[4] The lack of a centre of symmetry in wurtzite, combined with its large electromechanical coupling, results in strong piezoelectric and pyroelectric properties and the consequent use of ZnO in actuators,[5] piezoelectric sensors[6] and nanogenerators.[7] In addition, ZnO is a wide band-gap (3.37 eV) compound semiconductor with high exciton binding energy (60 meV), which ensures efficient excitonic ultraviolet (UV) emission at room temperature.[8] ZnO also exhibits the most diverse and

School of Materials Science and Engineering, Georgia Institute of Technology, Atlanta, GA 30332-0245, USA.
E-mail: zhong.wang@mse.gatch.edu
† The HTML version of this article has been enhanced with colour images.

Zhong Lin Wang

Dr Zhong Lin (ZL) Wang is a Regents' Professor, COE Distinguished Professor and Director, Center for Nanostructure Characterization and Fabrication, at Georgia Tech. He has authored and co-authored four scientific reference and textbooks and over 440 peer reviewed journal articles, 45 review papers and book chapters, edited and co-edited 14 volumes of books on nanotechnology, and holds 12 patents and provisional patents. He is in the world's top 25 most cited authors in nanotechnology from 1992 to 2002. His entire publications have been cited over 14 000 times.

Xudong Wang

Dr Xudong Wang received his PhD degree in MSE from Georgia Tech in 2005. He is currently a Postdoctoral Fellow working on designing, assembling and testing piezoelectric nanowire based devices. He developed a low-cost large-area self-assembly technique in aligning and patterning nanowires and nanoparticles. He has published more than 20 papers and holds 4 patents/provisional patents with Dr Zhong L. Wang in patterning nanostructures and designing nanodevices.

Jinhui Song

Jinhui Song holds a MS degree in physics and is currently a PhD candidate in the school of Materials Science and Engineering in Georgia Tech. He first discovered the mechanical–electrical energy converting phenomenon in ZnO nanowires and has been focused on developing nanowire-based piezoelectronic devices.

abundant configurations of nanostructures known to date, such as nanowires (NW),[9] nanobelts (NB),[10] nanosprings,[11] nanorings,[12] nanobows[13] and nanohelices.[14]

We have previously reviewed the formation of these novel nanostructures and the general synthesis methods.[15] In this review, we devote our focus to the aligned arrays of ZnO nanowire and nanobelt arrays, covering from synthesis to properties and to novel nanodevices. We will focus on the electronic devices, optoelectronic devices and the nanogenerators based on aligned nanowires and nanobelts.

1. Aligned growth of ZnO nanowire arrays

With the discovery of new or enhanced properties on functional NW structures, a diversity of novel applications has been proposed or even realized in the laboratory in the fields of optics,[16,17] electronics,[18] mechanics[19] and biomedical sciences.[20,21] However, assembling nanowires into devices is still challenging because of the difficulties in manipulating structures of such small sizes. New tools and approaches must be developed to meet new challenges. Aligned growth of nanowires is a simple but very efficient self-assembly technique for integrating nanowires into nanodevices,[22] such as nanowire lasers,[8] LEDs[23] or FETs.[24] In this section, the mechanisms and techniques for aligning ZnO nanowires are introduced and discussed.

1.1 Alignment of ZnO nanowires

The large-scale perfect vertical alignment of ZnO nanowires was firstly demonstrated on *a*-plane ($(11\bar{2}0)$ crystal surface) orientated single-crystal aluminium oxide (sapphire) substrates in 2001.[8] The general idea of this technique is to use gold nanoparticles as catalysts, in which the growth is initiated and guided by the Au particle and the epitaxial relationship between ZnO and Al_2O_3 leads to the alignment.

Unlike the normal vapor–liquid–solid (VLS) process, a moderate growth rate is required for the alignment since the catalyst needs to be molten, form alloys and precipitate step by step to achieve the epitaxial growth of ZnO on the sapphire surface. Therefore, a relatively low growth temperature was always applied to reduce the vapor concentration. Mixing ZnO with carbon powder, which is so-called carbon–thermal evaporation, can reduce the vaporization temperature from 1300 °C to 900 °C,

$$\mathrm{ZnO(s)} + \mathrm{C(s)} \xleftrightarrow{900\ ^\circ\mathrm{C}} \mathrm{Zn(v)} + \mathrm{CO(v)} \qquad (1)$$

The above reaction is reversible at a relatively lower temperature. So when the Zn vapor and CO were transferred to the substrate region, they could react and reform ZnO, which could be absorbed by the gold catalyst and eventually formed ZnO NWs through the VLS process. The detailed growth conditions can be found in our previous publications.

The typical morphology of the aligned ZnO NWs on a sapphire substrate is shown in Fig. 1a, a SEM image recorded at a 30° tilted view. All of the NWs are perpendicular to the substrate surface and the darker dot on the top of each nanowire is the gold catalyst. In this process, the growth spots

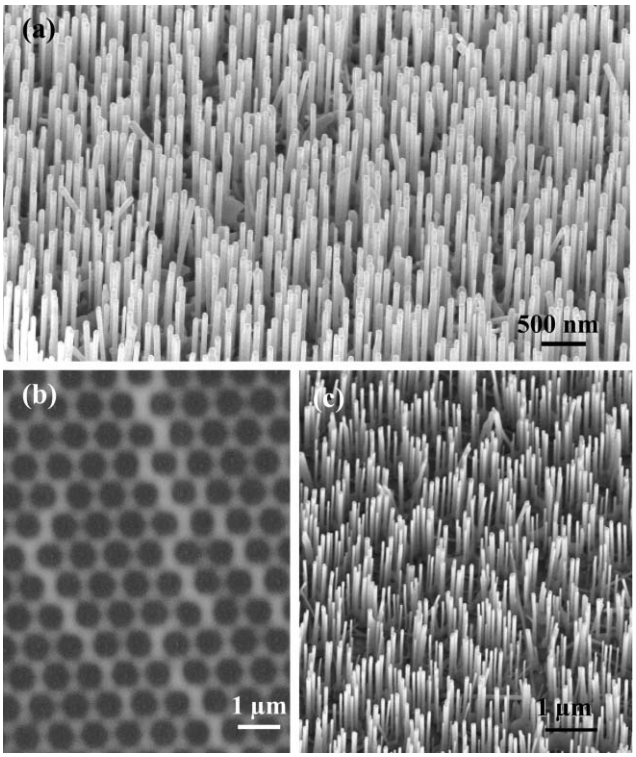

Fig. 1 (a) SEM image of aligned ZnO nanowires grown on a sapphire substrate using a thin layer of gold as catalyst. (b) SEM image of gold catalyst patterns using a PS sphere monolayer as a mask. (c) SEM image of aligned ZnO nanorods grown with a honeycomb pattern.

were dictated by the existence of the catalyst. If the applied catalyst was just a thin layer of gold, the distribution of the NWs would be random (Fig. 1a). The catalyst can also be pre-patterned by lithography or self-assembly techniques. For example, a two-dimensional, large-area, self-assembled and ordered monolayer of submicron polystyrene spheres was formed on a sapphire substrate as a mask, through which a thin layer of gold was deposited. After etching away the spheres, a hexagonal network of gold layer was achieved (Fig. 1b),[25] catalyzed by which, the as-grown aligned NWs exhibited the same honeycomb-like distribution (Fig. 1c).

1.2 Epitaxial relationships

Aligned ZnO NWs have been successfully grown on sapphire, GaN, AlGaN and AlN substrates[26,27] through a VLS process, where the crystal structure of the substrate is crucial for the orientation of NWs. An epitaxial relationship between the substrate surface and ZnO nanowires determines whether there will be aligned growth and how good the alignment can be. NWs grown on silicon substrates are always randomly orientated because the gold catalyst tends to form an alloy with silicon at relatively low temperature and destroys the single-crystalline silicon surface.[9] The successful alignment of ZnO NWs on sapphire and nitride substrates is attributed to the very small lattice mismatches between the substrates and ZnO.

In the case of sapphire, a $(11\bar{2}0)$ plane orientated substrate is always used because the smallest lattice mismatch is along

the *c*-axis of Al_2O_3 and the *a*-axis of ZnO. The epitaxial relationship between a ZnO NW and an *a*-plane sapphire substrate is schematically shown in Fig. 2a, where $(0001)_{ZnO} \parallel (11\bar{2}0)_{Al_2O_3}$, $[11\bar{2}0]_{ZnO} \parallel [0001]_{Al_2O_3}$. The lattice mismatch between $4[01\bar{1}0]_{ZnO}$ ($4 \times 3.249 = 12.996$ Å) and $[0001]_{Al_2O_3}$ (12.99 Å) is almost zero, which confined the growth orientation of ZnO NWs. Nevertheless, since the $(11\bar{2}0)$ plane of Al_2O_3 is a rectangular lattice but the (0001) plane of ZnO is a hexagonal lattice, this epitaxial relationship can only hold in one direction. As illustrated in Fig. 2a, along the $[1\bar{1}00]$ direction, the lattice mismatch is fairly large, which will introduce some distortion on their lattices and cause stresses around the interface. As a result, the lateral growth of ZnO side branches was always observed for *a*-plane sapphire substrates, especially on the edge of the growth area, where there is no space restriction for lateral growth (Fig. 2b).

As for the nitride substrates, GaN, AlN and AlGaN all have the same wurtzite structure as ZnO. So, the deposited ZnO NWs are confined to their six equivalent $<01\bar{1}0>$ directions and only grow along the [0001] direction, exactly following the substrate's crystal orientation, as shown in Fig. 3a. In this case, the epitaxial confinement is evenly distributed along the entire 2D atomic plane. As a result, even though the lattice mismatch becomes larger and larger from GaN (1.8%) to AlN (4.3%), the aligned growth was still kept very well and the possibility for ZnO nanorods to undergo lateral growth is rare (Fig. 3b). Therefore, *c*-plane oriented $Al_xGa_{1-x}N$ substrates are ideal for the growth of aligned ZnO NWs.

1.3 Growth condition control

The growth direction is controlled by the epitaxial relationship between the substrate and NWs; while the aligning quality is controlled by many other factors. We have performed a systematic investigation on the growth conditions, which were generalized into three basic terms: chamber pressure, oxygen partial pressure[28] and thickness of catalyst layer.[29]

From the experiment results, we found the oxygen partial pressure and the system total pressure played key roles in the growth of ZnO nanowires. With different oxygen volume percentage and different chamber pressure, the quality and growth behavior of the ZnO nanowires are strongly affected. We have carried out over 100 growth experiments under different growth conditions, which were designed to quantitatively define the best combination of the O_2 partial pressure and the chamber pressure for the growth of aligned ZnO nanowires. For consistency, all of the samples were collected at the 880 °C temperature zone, which is 10 cm away from the source materials. The O_2 volume percentage in the chamber varied from 1 to 4 vol%, and the system pressure varied from 1.5 to 300 mbar.

The experimental results are summarized in Fig. 4, which is a "growth diagram" for the O_2 volume percentage in the chamber and system pressure, under which the optimum conditions for growing aligned ZnO nanowires are presented. The term of "growth diagram" used here is given a new

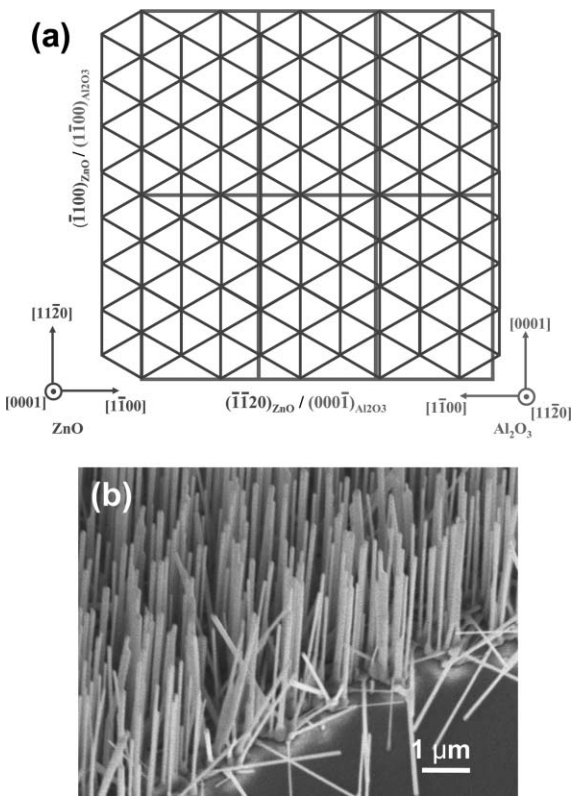

Fig. 2 (a) Schematic of the epitaxial relationship between the *c*-plane of ZnO and the *a*-plane of Al_2O_3. (b) Edge region image of the aligned ZnO nanowires grown on a sapphire substrate.

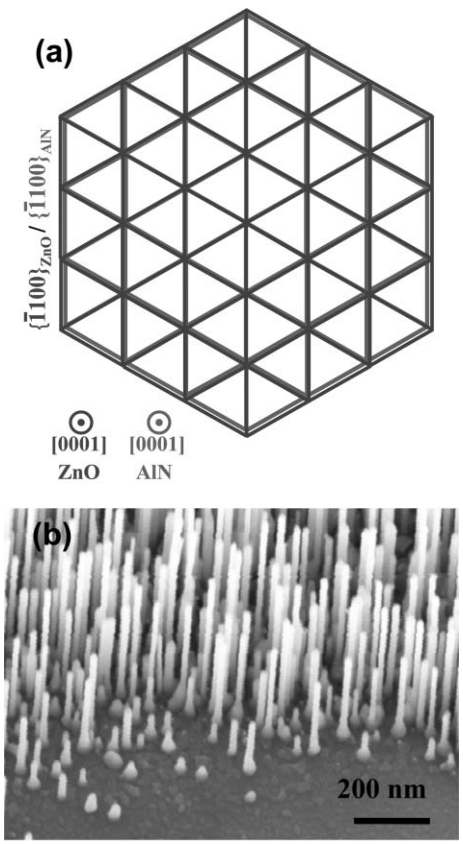

Fig. 3 (a) Schematic of the epitaxial relationship between the *c*-plane of ZnO and the *c*-plane of AlN. (b) Edge region image of the aligned ZnO nanowires grown on an AlN substrate.

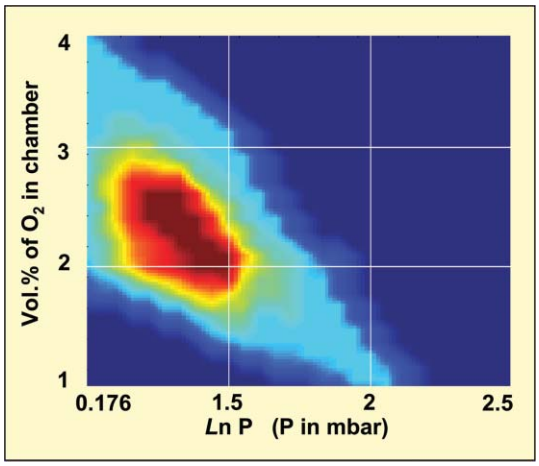

Fig. 4 "Growth diagram" that correlates oxygen volume percentages in the growth chamber (*e.g.* partial pressure) and the growth chamber pressure (plotted in logarithm and *P* is in mbar) for growing aligned ZnO nanowires. The point matrix was broadened and smoothed by MatLab to form a quasi-continuous phase diagram.

meaning of representing the "road map" for controlled synthesis of nanowires. This phase diagram was determined for the single-zone tube furnace vapor deposition system. As shown in Fig. 4, the horizontal axis is the logarithm of the total chamber pressure; the vertical axis is the oxygen volume percentage in the chamber, and the quality of the grown ZnO nanowires is represented by different colors. The quality of the nanowires is characterized by their uniformity, density, length, and alignment. In the growth diagram, dark red represents the best growth conditions, where a perfect alignment of ZnO nanowires with a high density and uniform length and thickness were achieved. The growth is good in the red area, where the density is lower and the nanowires are shorter. In the green and light blue areas, the growth is poor, where only a small amount of short nanowires was found. No growth was found in the dark blue region. This growth diagram provides the road map for growing high quality aligned ZnO nanowires.

The catalyst effect on the alignment of ZnO NWs was also studied. By varying the thickness of the gold catalyst film, we found the density of aligned ZnO nanowires exhibited an almost linear relationship with the catalyst thickness. In the experiment, eight stripes of gold layer with thicknesses from 1 to 8 nm at 1 nm gradient were deposited onto a 2 cm × 1 cm $Al_{0.5}Ga_{0.5}N$ substrate through a thermal evaporation process. The fabrication of ZnO nanowires was carried out under the optimal experimental conditions. All of the nanowires were grown simultaneously and under identical experimental conditions. The inset in Fig. 5 is an optical picture of the substrate, from which the eight stripes can be clearly distinguished. From left to right, the color of the stripes varies from light blue to purple, which represent the aligned ZnO nanowires catalyzed by an Au layer of thickness from 1 to 8 nm. SEM analysis showed NW densities were changed according to the variation of catalyst thickness. Quantitative analysis was thereafter performed to reveal the density and thickness relationships of the aligned nanowires. The nanowire density at each thickness of gold catalyst layer is shown on the left-hand axis in Fig. 5

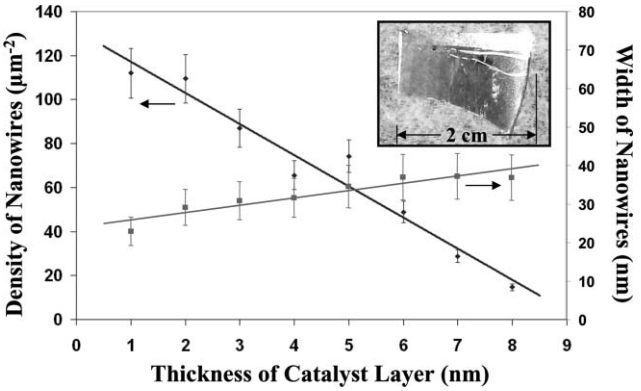

Fig. 5 Variation of density (left vertical axis) and width (right vertical axis) of the aligned ZnO nanowires with the thickness of gold catalyst layer. Inset: photo of the substrate showing eight stripes of the aligned ZnO nanowires with different densities.

with an average error of ~10%. An almost linear drop in density from 112 to 15 μm^{-2} with increasing catalyst thickness can be observed. However, unlike the density, the average width of NWs remains between 30 and 40 nm despite the change in catalyst thickness. Owing to the linear relationship between the density of NWs and the thickness of the catalyst layer, thickness control of the gold catalyst could be a very simple and effective way to achieve density control of aligned NWs over a large surface area.

2. Properties investigation on ZnO nanowires and nanobelts

The vertically aligned morphology enabled a much easier manipulation and properties characterization of ZnO NWs. The optical or electrical responses are expected to be enhanced along the aligned direction instead of being cancelled out by a random distribution. Therefore, experiments were performed on the ZnO NWs and NBs to reveal their morphology- and structure-induced novel mechanical, electrical and optical properties.

2.1 Elastic properties of aligned ZnO nanowires

Based on the aligned ZnO NWs, we have recently demonstrated an AFM based technique for measuring the elastic properties of individual ZnO NWs.[19] By simultaneously recording the topography and lateral force image in AFM contact mode when the AFM tip scans across the aligned nanowire arrays, the elastic modulus of individual NWs is determined. This technique allows a measurement of the mechanical properties of individual NWs of different lengths in an aligned array without destroying or manipulating the sample.

The principle for the AFM measurement is illustrated in Fig. 6a. In AFM contact mode, a constant normal force is kept between the tip and sample surface. The tip scans over the top of the ZnO NW and the tip's height is adjusted according to the surface morphology and local contacting force. Before the tip meets a NW, a small lateral force is observed (Fig. 6a I). When the tip comes into contact with a NW, the lateral force increases almost linearly as the NW is elastically bent from its

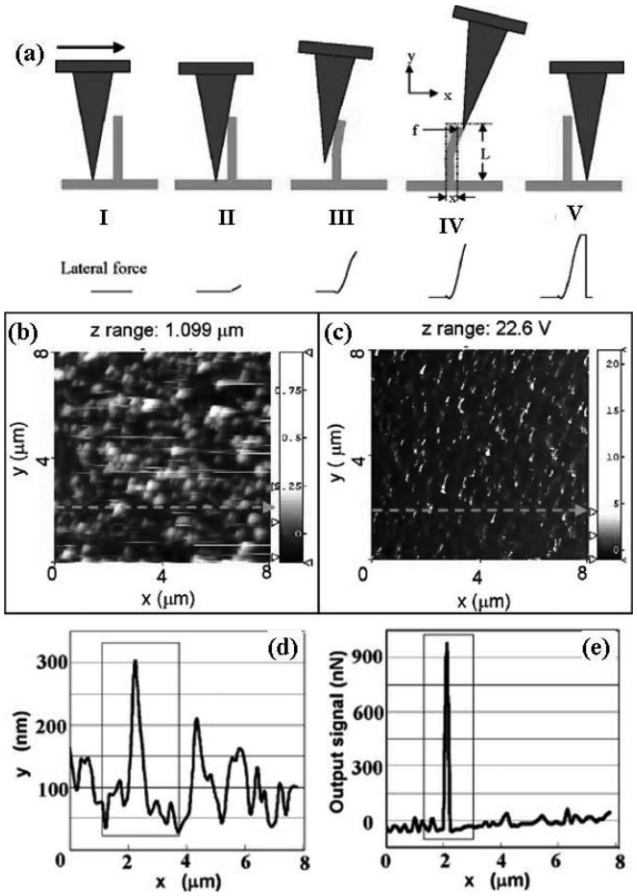

Fig. 6 (a) Procedure for measuring the elastic modulus of a NW in the AFM contact mode. (b) Topography image and (c) lateral force image of the aligned ZnO NWs received in AFM contact mode. (d, e) Line scanning profiles along the dashed lines in b and c, respectively.

equilibrium position (Fig. 6a II and III). At the largest bending position, as illustrated in Fig. 6a IV, the tip crosses the top of the NW, then the NW is released; the lateral force drops suddenly and reaches the ordinary level (Fig. 6a V)

The elastic modulus is derived based on the following calculation. From the geometrical relationship illustrated in Fig. 6a IV, when a vertical NW experiences a lateral force f parallel to the scanning direction, the force f can be expressed as:

$$f = 3EI\frac{x}{L^3} \tag{2}$$

where E and I are the elastic modulus and momentum of inertia of the NW, x is the lateral displacement perpendicular to the NW, and L is the length of the NW. From Hook's law, the spring constant is $K = f/x$. For a ZnO NW with a hexagonal cross-section, its moment of inertia is $I = (5(3^{1/2})/16)a^4$, where a is the radius of the NW. Therefore, the elastic modulus is given by:

$$E = \frac{16L^3K}{15\sqrt{3}a^4} \tag{3}$$

The displacement and the lateral force were determined from the topography image and the corresponding lateral force image, as shown in Fig. 6b and c, respectively. To ensure that the center of the conical tip touches the center of the NW as assumed in theoretical calculations, both curves were read from the center of the NW as indicated in the images by dashed lines. Taking a line scan across the middle point of a spot in the topography image, a curve for the scanner retracting distance *versus* the NW lateral displacement was obtained, as shown in Fig. 6d. Likewise, the maximum lateral force for bending the NW was measured by taking a scanning profile at the corresponding line in the lateral force image (as indicated in Fig. 2e). Combining the measured x_m and f_m from the two line profiles, the spring constant $K = f_m/x_m$ was obtained. For the ZnO nanowires grown on sapphire surfaces with an average diameter of 45 nm, the elastic modulus was determined to be 29 ± 8 GPa. This technique provided a direct observation of the mechanical properties of aligned NWs, which is of great importance for their applications in electronics, optoelectronics, sensors, and actuators.

2.2 Elastic deformation behavior of bridged nanobelts

After knowing the elastic modulus of ZnO NWs, another approach was developed to quantify the elastic deformation behavior along such 1D nanostructures. The experiment was carried out by scanning a suspended NB along its length direction using an AFM tip in contact mode at a constant applied force.[30] As shown in Fig. 7a, a ZnO NB was manipulated across a trench etched on a silicon substrate. A series of bending images of the NB were recorded by changing the magnitude of the AFM contact force. After eliminating the effects of surface roughness and initial bending of the NB on force curve quantification, the normalized profiles of a suspended NB along the length direction under different contact forces are shown in Fig. 7b.

The profile images of the NB recorded the deformation of all of the points along its length under different applied forces. One profile contains up to 650 points, each of which can be regarded as a mechanical measurement. However, there are two typical models derived under different boundary conditions—clamped–clamped beam model (CCBM), where the two ends of the NB are fixed; and free–free beam model (FFBM), where the two ends of the NB can freely slide. In the literature,[31] the CCBM was usually assumed to be applied on 1D nanostructures due to large contact surfaces but there is a lack of sufficient data to support this fact. By fitting the shape of the curve measured experimentally under different applied forces, the model that is more precise to quantify the elastic deformation behavior of the NB was reliably determined. Fig. 7c shows an example of curve fitting based on the two models. The FFBM is found to fit much better than the CCBM, especially when the applied force is large (>190 nN). Therefore, in our case, the adhesion force and the force moment at each side of the NB are negligible and the FFBM is the most reasonable model in explaining the mechanical deformation.

2.3 ZnO nanobelt/nanowire Schottky diodes

Besides the mechanical properties, in order to apply ZnO nanostructures to various electronic devices, it is important to

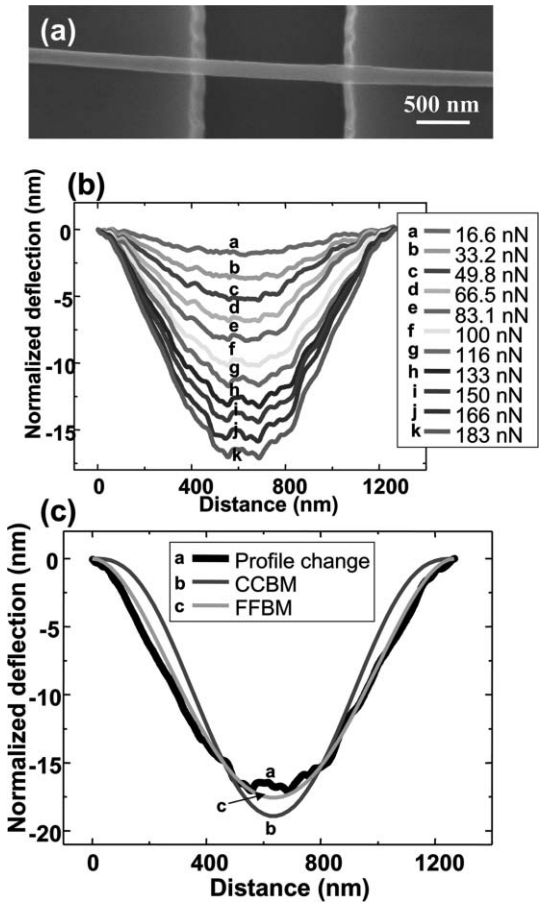

Fig. 7 (a) SEM image of one NB bridged over a trench. (b) The normalized AFM image profile after removing the surface roughness by subtracting the curve acquired at 106 nN; the force is also normalized in reference to the "zero setting point" of 106 nN. (c) Curve fitting using the CCBM and FFBM for the image profiles of the NB acquired under a normalized force of 183 nN.

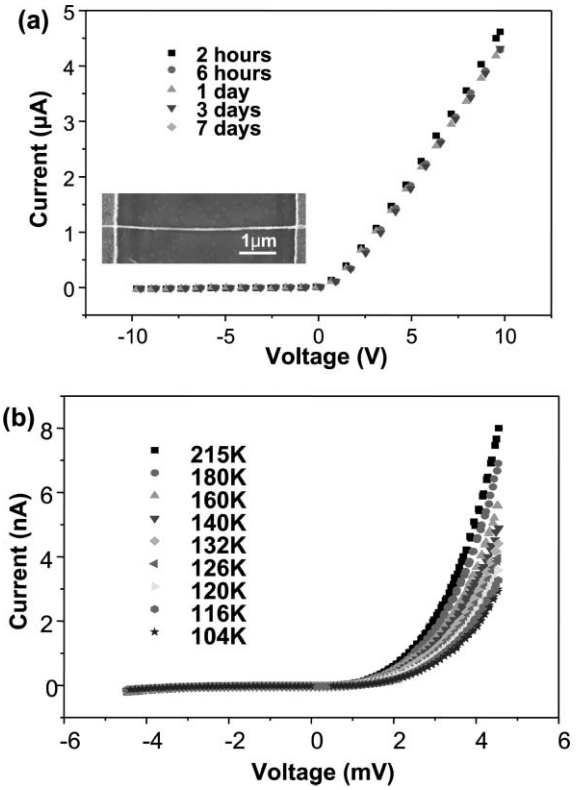

Fig. 8 (a) Rectifying *IV* characteristics of a single ZnO nanobelt lying on Au electrodes at different times after the fabrication, showing the stability of the device. Inset is the SEM image of the ZnO nanobelt device. (b) *IV* characteristics of the Schottky diode at different temperatures showing the semiconducting behavior.

understand its transport properties and its interaction with metal contacts. By aligning single ZnO nanobelts/nanowires across paired Au electrodes using dielectrophoresis, rectifying diodes of single nanobelt/nanowire-based devices were fabricated to reveal their electronic properties.[32] In the device fabrication, a droplet of the nanobelt suspension was applied onto prefabricated electrodes, which were connected to a 5 V and 1 MHz AC signal. The electrical polarization force aligned the nanobelts across two electrodes. By controlling the concentration of the nanobelt suspension, a circuit with only one single nanobelt has been made (inset of Fig. 8a).

Electric measurement revealed that the *IV* characteristics of such devices displayed a rectifying behavior as shown in Fig. 8a. Data correspond to different measurements of the same device at different time intervals after the device was made. The last measurement was performed 7 days after the device was exposed to air. It is consistent with the data obtained 2 h after the sample was made, showing that the rectifying behavior of the nanodevices is very stable. The temperature dependence of the diode was also measured (Fig. 8b). The current under the forward bias decreased with decreasing temperature. The resistivity of the nanobelt increased by a factor of 2 when the temperature decreased from 215 to 104 K, showing a typical semiconductor *IV* characteristic. When the temperature was below 50 K, the carrier transportation was depressed greatly. The device acted like an open circuit with a resistivity greater than 10^5 Ω cm. From the *IV* characterization, the device exhibited some superb properties. The current flowing through the diode was ~0.5 μA at 1.5 V forward bias, which was about 100 times larger than similar devices reported earlier.[33] The ideality factor for our devices was ~3 and the on-to-off current ratio was as high as 2000, indicating good performance of our devices.

The diode effect could be a result of the asymmetric contacts between the ZnO nanobelts and the Au electrodes. The ZnO–Au contact is usually a Schottky contact, so there should be no rectifying behavior if the contacts are symmetrical. However, in the dielectrophoresis deposition process, the contacts of the nanobelt's two ends were made one after another onto the corresponding electrodes. We suspect that the first touched side may have had a firm contact with the electrode and formed a better contact with lower barrier height; whereas the other end that contacted later had a higher barrier, possibly leading to the formation of the Schottky diode for our devices. It has also been found that the spontaneous formation of the Au/ZnO nanobelt diodes depends strongly on the sizes of the nanobelts. For the nanobelts with smaller sizes (<200 nm), Schottky diodes are preferentially formed.

2.4 Oxygen diffusion in ZnO nanobelts

The as-grown ZnO nanostructure is a naturally n-type semiconductor and its electronic properties strongly rely on the oxygen deficiency and distribution in the structures. Therefore, investigation of oxygen diffusion was performed on a ZnO nanobelt device.[34] For this purpose, a ZnO nanobelt was placed between two Au electrodes and subsequently coated by a 50 nm Si_3N_4 layer to isolate the ZnO nanobelt from contacting the atmosphere. Half of the deposited Si_3N_4 was then milled off by a focussed ion beam (FIB) for oxygen absorption, as shown schematically in Fig. 9a. The current–voltage characteristics of the ZnO nanobelt device (inset of Fig. 9b) were then measured on a daily basis throughout one week. The measured conductivity changes on two such samples as a function of time are shown in Fig. 9b. It was found that the conductivity dropped almost linearly with increasing number of days when the ZnO nanobelt was exposed to air.

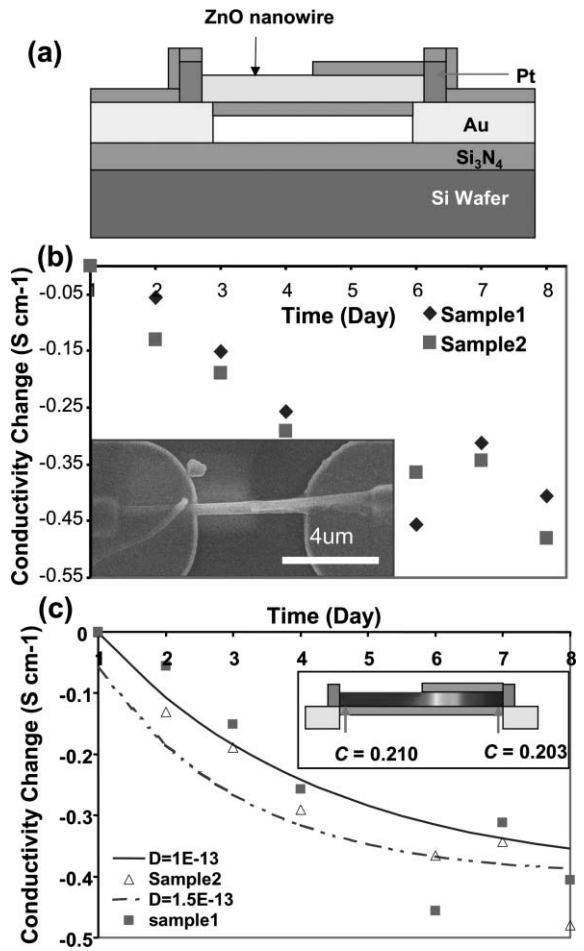

Fig. 9 (a) Schematic of ZnO nanowire placed on pre-patterned Au electrodes after Si_3N_4 deposition. (b) Conductivity change of ZnO nanowires over time. The inset shows the SEM image of the device. (c) Illustration of curve fitting to determine the oxygen diffusion coefficient. The continuous lines represent the simulated results while the symbols represent the experimental results. The inset shows simulated oxygen distribution on the eighth day after the ion milling process.

In order to explain the behavior of the observed conductivity change, a simulation of the oxygen diffusion was constructed by assuming: (1) a uniform distribution of defects along the nanobelt's volume; (2) oxygen molecules adhered to the surface of ZnO broke down to single oxygen atoms, which remained at the same molecular concentration as the oxygen molecules in atmosphere; and (3) no oxygen diffused through the Si_3N_4 insulating layer. The inset of Fig. 9c illustrates the oxygen concentration distribution profile on the eighth day. Based on semiconductor theory, the conductivity in n-type ZnO can be given by:

$$\Delta\sigma(t) \approx -2e\mu_e\Delta C_O(t) \quad (4)$$

where $\Delta\sigma(t)$ is the conductivity change of ZnO as a function of time, e is the charge of an electron, μ_e is the electron mobility in ZnO and $\Delta C_O(t)$ is the concentration change of oxygen vacancies due to diffusion. $\Delta C_O(t)$ could be obtained from simulation, and μ_e is known for ZnO nanowires/nanobelts through a previous measurement to be around 17 $cm^2\ V^{-1}\ s^{-1}$.[35] So it is possible to plot a curve of conductivity *versus* time change as shown in Fig. 9c. By comparing the experimentally measured conductivity and that simulated using finite element analysis (FEA), we were able to derive the diffusion coefficient of oxygen in ZnO nanowires/nanobelts.

2.5 Light emitting properties

The light emitting properties of aligned ZnO nanowires were characterized by measuring the photoluminescence (PL) spectra under different detecting angles and different densities.[25] All of the PL measurements were performed at room temperature. The angular PL measurements were carried out on the hexagonal patterned aligned ZnO nanowires grown on a sapphire substrate. The excitation laser beam was incident onto the sample at an angle of 45°, while the detection angle was defined as the angle between the detector and the direction normal to the substrate, as shown in the inset in Fig. 10a. The emission spectra were recorded at four different detection angles: 0°, 15°, 30° and 45° (Fig. 10a). The aligned ZnO nanowires exhibit a peak at 384 nm at $\theta = 0°$. As the detection angle was increased, the luminescence intensity dropped dramatically, which indicates that the luminescence was emitted mainly along the direction perpendicular to the substrate. Moreover, the luminescence peak shifted very slightly from 384 nm to 383 nm when the detection angle increased from 0° to 45°. This may also be caused by the polarization of the emitted light from the aligned nanowires.[36]

In order to reveal the density related light emitting properties, PL measurements were performed on the aligned ZnO nanowires catalyzed by a gold layer with a thickness from 1 to 8 nm,[29] which induced density variances as shown in section 1.3. Strong luminescence peaks are observed at 377 nm from all of the eight curves, while the intensities are varied, as shown in Fig. 10b. This is consistent with the constant diameter of the nanowires for all of the samples. In general, the intensity decreased when the density was decreasing, as shown in the inset of Fig. 10b. The highest intensity is from the nanowires catalyzed by a 1 nm gold layer, which has the

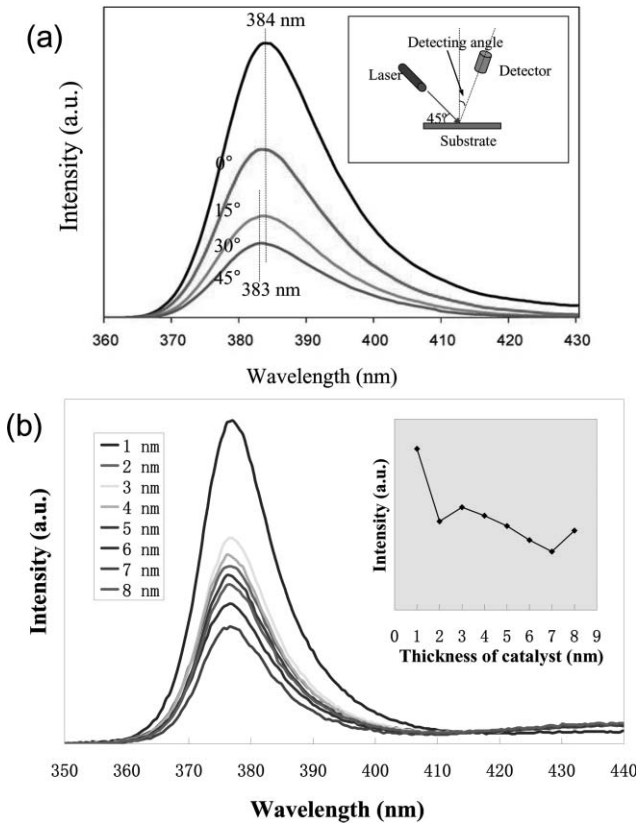

Fig. 10 (a) PL spectra acquired from an aligned ZnO nanowire array grown on a sapphire substrate as a function of the angle between the detector and a direction normal to the substrate. The inset shows the measurement set-up. (b) PL spectra of the eight stripes of the aligned ZnO nanowires with decreasing densities that were catalyzed by a gold layer from 1 to 8 nm thick. Inset: variation of the intensity of PL peaks with the change of catalyst thickness.

highest density as well. However, the lowest intensity is not from the sample with the lowest density. The sample catalyzed by 8 nm gold shows an enhancement of its luminescence intensity. This is probably owing to the increased reflectivity of the emitted light by the large gold particles lying on the substrate. The increase of intensity from samples catalyzed by 2 to 3 nm thick gold may also be attributed to the increased reflectivity due to the formation of a continuous ZnO bottom layer.

3. Novel nanodevices based on ZnO nanowire/nanobelt arrays—nanogenerators

ZnO is a unique material that simultaneously exhibits semiconducting and piezoelectric properties. The coupling of these two properties can realize some unique functions that can never been achieved by other materials. In this section, we will introduce nanogenerators based on aligned ZnO NWs exploring those novel functions.

Using piezoelectric ZnO NW arrays, we have discovered an innovative phenomenon on converting nano-scale mechanical energy into electric energy.[7,37] The measurements were performed by AFM using a Si tip coated with Pt. In the AFM contact mode, a constant normal force of 5 nN was

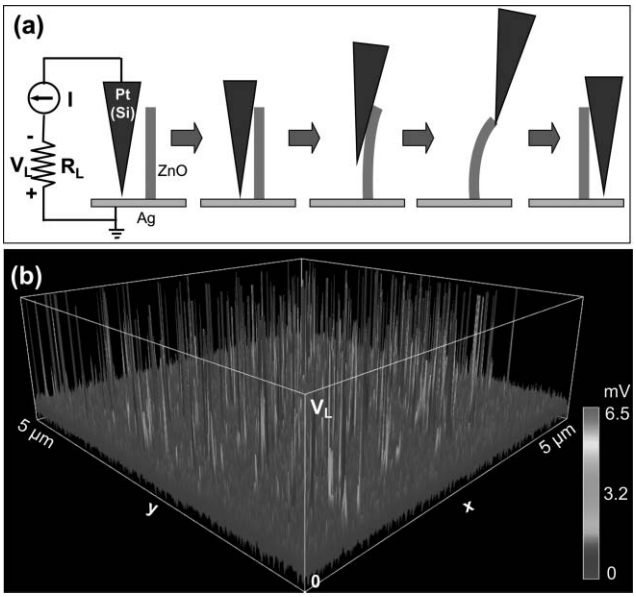

Fig. 11 (a) Experimental set-up and procedures for generating electricity by deforming a piezoelectric NW using a conductive AFM tip. (b) Output voltage image map of ZnO NW arrays.

maintained between the tip and sample surface. The tip scanned over the top of the ZnO NWs, which were thus bent and then released. The output voltage across an outside load of resistance R_L = 500 MΩ was continuously monitored while the tip scanned over the nanowires, as shown in Fig. 11a. Meanwhile, the corresponding output voltages across the load were recorded. In the output voltage image shown in Fig. 11b, many sharp output voltage peaks (like discharge peaks) were observed, which are typically about 4–50 times higher than the noise level, and most of the voltage peaks were ~6–9 mV in height. The density of NWs contacted by the tip was counted to be ~20 μm^{-2}, and the average density of NWs whose voltage output events had been captured by the tip is ~8 μm^{-2}, thus ~40% of the NWs were contacted.

The physical principle for creating the piezoelectric discharge energy is related to the uniquely coupled piezoelectric and semiconducting dual properties of ZnO. For a vertical straight ZnO NW (Fig. 12a), the deflection of the NW by the AFM tip creates a strain field, with the outer surface (right-hand side) being stretched (positive strain ε) and inner surface (right-hand side) compressed (negative strain ε) (Fig. 12b). Due to the electric–mechanical coupling characteristic of ZnO, an electric field E_z along the NW (z direction) will be created inside its volume due to the piezoelectric effect, $E_z = \varepsilon_z/d_{33}$, where d_{33} is the piezoelectric coefficient along the nanowire direction that is normally the positive c-axis with the Zn atomic layer being the front terminating layer.[38] The piezoelectric field direction is closely parallel to the z-axis (NW direction) at the outer surface and anti-parallel to the z-axis at the inner surface (Fig. 12c). Under the first order approximation, across the width of the NW at the top end, the electric potential distribution from the left-hand side surface (compressed) to the right-hand side surface (stretched) is approximately between V_s^- to V_s^+ ($V_s^{\mp} = \mp 3Ty_m/4Ld_{33}$, where T, L and y_m are the thickness, length and maximum deflection of

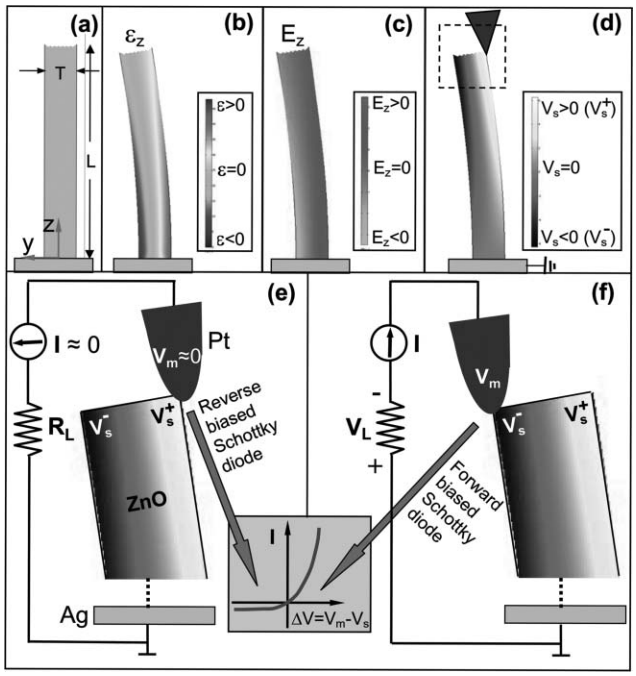

Fig. 12 (a) Schematic definition of a NW and the coordination system. (b) Longitudinal strain distribution in the NW after being deflected. (c) The corresponding longitudinal piezoelectric induced electric field E_z distribution in the NW. (d) Potential distribution in the NW as a result of piezoelectric effect. (e, f) Metal–semiconductor (M–S) contacts between the AFM tip and the ZnO NW at two reversed local contact potentials (positive and negative).

the NW). The electrode at the root of the NW is grounded. The potential is created by the relative displacement of the Zn^{2+} cations with respect to the O^{2-} anions due to the piezoelectric effect in the wurtzite crystal structure; thus, these ionic charges cannot freely move and cannot recombine without releasing the strain (Fig. 12d). The potential difference is maintained as long as the deformation is in place and no foreign free charges (such as from the metal contacts) are injected.

In experimental design, the contacts at the top and the root of the NW were non-symmetric. The contact at the bottom was between ZnO and silver paste, which was ohmic. At the tip of the NW, however, the contact between Pt and ZnO was Schottky, which dominates the entire transport process. In the first step, the AFM conductive tip that induces the deformation is in contact with the stretched surface of positive potential V_s^+ (Fig. 12d and e). Since the Pt metal tip has a potential of nearly zero, $V_m = 0$, the metal tip–ZnO interface is negatively biased for $\Delta V = V_m - V_s^+ < 0$. With consideration of the n-type semiconductor characteristic of the as-synthesized ZnO NWs, the Pt metal/ZnO semiconductor (M–S) interface in this case is a reverse biased Schottky diode (Fig. 12e), resulting in little current flowing across the interface. In the second step, when the AFM tip is in contact with the compressed side of the NW (Fig. 12f), the metal/ZnO interface is positively biased for $\Delta V = V_L = V_m - V_s^- > 0$. The M/S interface in this case is a positively biased Schottky diode, resulting in a sudden increase in the output electric current, *e.g.*, a sharp increase in output voltage V_L (positive). The current is the result of ΔV driven flow of electrons from the semiconductor ZnO NW to the metal tip. The flow of the free electrons from the loop through the NW to the tip will neutralize the ionic charges distributed in the volume of the NW and thus reduce the magnitude of the potential V_s^- and V_s^+. Therefore, the output voltage V_L starts to drop and reaches zero until all of the ionic charges in the NW are fully neutralized. It is also important to note that the discharge occurs when the NW is bent nearly to the maximum deflection according to the model, which is in agreement with the observation. The principle demonstrated here is the fundamental mechanism of nano-piezotronics, a new field of utilizing piezoelectric effect for fabricating unique and novel electromechanically coupled electronic devices and components.

4. Summary

Aligning nanostructures through a low-cost self-assembly process is showing great potential in nano-device fabrication and integration. It is very likely to bring current idea-proof nano-devices from scientific models to commercial products once the assembly mechanisms are better understood. Moreover, the aligned and ordered configurations of nanostructures can also induce enhanced properties and new applications. This paper reviews the growth techniques for aligning ZnO NWs and the growth conditions effects on the alignment quality. Properties of 1D ZnO nanostructures, such as bending modules, electron transport and PL, are discussed based on their aligned morphology and individual nanostructures. Owing to the semiconducting and piezoelectric dual properties of ZnO crystals, novel applications are induced using aligned ZnO NWs, such as nanogenerators. Those unique properties and applications will have profound impacts in many areas, such as self-powered nanodevices and nanosystems for *in situ*, real-time and implantable biosensing and biodetection, self-powering for defence and commercial applications, and remote sensing for space technology.

Acknowledgements

Thanks to Y. Ding, P. X. Gao, R. S. Yang, C. S. Lao, W. L. Hughes, B. Buchine, W. J. Mai, J. Liu, C. Ma and J. Zhou for their contributions to the work reviewed in this article. We acknowledge generous support from DARPA, NSF, NASA and NIH.

References

1 C. M. Lieber, *MRS Bull.*, 2003, **28**, 486–491.
2 R. S. Friedman, M. C. McAlpine, D. S. Ricketts, D. Ham and C. M. Lieber, *Nature*, 2005, **434**, 1085.
3 Z. L. Wang, *Nanowires and Nanobelts: Materials, Properties and Devices. Metal and Semiconductor Nanowires*, Kluwer Academic Publishers, Norwell, MA, 2003.
4 Ü. Özgür, Y. I. Alivov, C. Liu, A. Teke, M. A. Reshchikov, S. Doğan, V. Avrutin, S.-J. Cho and H. Morkoç, *J. Appl. Phys.*, 2005, **98**, 041301.
5 B. A. Buchine, W. L. Hughes, F. L. Degertekin and Z. L. Wang, *Nano Lett.*, 2006, **6**, 1155–1159.
6 X. D. Wang, J. Zhou, J. H. Song, J. Liu, N. S. Xu and Z. L. Wang, *Nano Lett.*, 2006, **6**, 2768–2772.

7 Z. L. Wang and J. H. Song, *Science*, 2006, **312**, 242–246.
8 M. Huang, S. Mao, H. Feick, H. Yan, Y. Wu, H. Kind, E. Weber, R. Russo and P. Yang, *Science*, 2001, **292**, 1897–1899.
9 M. H. Huang, Y. Wu, H. Feick, N. Tran, E. Weber and P. Yang, *Adv. Mater.*, 2001, **13**, 113–116.
10 Z. W. Pan, Z. R. Dai and Z. L. Wang, *Science*, 2001, **291**, 1947–1949.
11 X. Y. Kong and Z. L. Wang, *Nano Lett.*, 2003, **3**, 1625–1631.
12 X. Y. Kong, D. Yong, R. Yang and Z. L. Wang, *Science*, 2004, **303**, 1348–1351.
13 W. L. Hughes and Z. L. Wang, *J. Am. Chem. Soc.*, 2004, **126**, 6703–6709.
14 P. X. Gao, Y. Ding, W. Mai, W. L. Hughes, C. S. Lao and Z. L. Wang, *Science*, 2005, **309**, 1700–1704.
15 Z. L. Wang, *J. Phys.: Condens. Matter*, 2004, **16**, R829–R858.
16 X. Duan, Y. Huang, Y. Cui, J. Wang and C. M. Lieber, *Nature*, 2001, **409**, 66–69.
17 F. Qian, S. Gradecak, Y. Li, C. Wen and C. M. Lieber, *Nano Lett.*, 2005, **5**, 2287–2291.
18 Y. Huang, X. Duan, Y. Cui, L. Lauhon, K. Kim and C. M. Lieber, *Science*, 2001, **294**, 1313–1317.
19 J. H. Song, X. D. Wang, E. Riedo and Z. L. Wang, *Nano Lett.*, 2005, **5**, 1954–1958.
20 F. Patolsky and C. M. Lieber, *Mater. Today*, 2005, **8**, 20–28.
21 F. Patolsky, B. P. Timko, G. Yu, Y. Fang, A. B. Greytak, G. Zheng and C. M. Lieber, *Science*, 2006, **313**, 1100–1104.
22 H. J. Fan, P. Werner and M. Zacharias, *Small*, 2006, **2**, 700–717.
23 W. I. Park and G. C. Yi, *Adv. Mater.*, 2004, **16**, 87–90.
24 J. Goldberger, A. Hochbaum, R. Fan and P. Yang, *Nano Lett.*, 2006, **6**, 973–977.
25 X. D. Wang, C. J. Summers and Z. L. Wang, *Nano Lett.*, 2004, **4**, 423–426.
26 X. D. Wang, J. H. Song, P. Li, J. H. Ryou, R. D. Dupuis, C. J. Summers and Z. L. Wang, *J. Am. Chem. Soc.*, 2005, **127**, 7920–7923.
27 H. J. Fan, F. Fleischer, W. Lee, K. Nielsch, R. Scholz, M. Zacharias, U. Gosele, A. Dadgar and A. Krost, *Superlattices Microstruct.*, 2004, **36**, 95–105.
28 J. H. Song, X. D. Wang, E. Riedo and Z. L. Wang, *J. Phys. Chem. B*, 2005, **109**, 9869–9872.
29 X. D. Wang, J. H. Song, C. J. Summers, J. H. Ryou, P. Li, R. D. Dupuis and Z. L. Wang, *J. Phys. Chem. B*, 2006, **110**, 7720–7724.
30 W. J. Mai and Z. L. Wang, *Appl. Phys. Lett.*, 2006, **89**, 073112.
31 J. P. Salvetat, G. A. D. Briggs, J. M. Bonard, R. R. Bacsa, A. J. Kulik, T. Stockli, N. A. Burnham and L. Forro, *Phys. Rev. Lett.*, 1999, **82**, 944–947.
32 C. S. Lao, J. Liu, P. X. Gao, L. Zhang, D. Davidovic, R. Tummala and Z. L. Wang, *Nano Lett.*, 2006, **6**, 263–266.
33 O. Harnack, C. Pacholski, H. Weller, A. Yasuda and J. M. Wessels, *Nano Lett.*, 2003, **3**, 1097–1101.
34 J. Liu, P. X. Gao, W. J. Mai, C. S. Lao and Z. L. Wang, *Appl. Phys. Lett.*, 2006, **89**, 063125.
35 Z. Fan, D. Wang, P.-C. Chang, W.-Y. Tseng and J. G. Lu, *Appl. Phys. Lett.*, 2004, **85**, 5923–5925.
36 J. C. Johnson, H. Yan, P. Yang and R. J. Saykally, *J. Phys. Chem. B*, 2003, **107**, 8816–8828.
37 J. H. Song, J. Zhou and Z. L. Wang, *Nano Lett.*, 2006, **6**, 1656–1662.
38 Z. L. Wang, X. Y. Kong and J. M. Zuo, *Phys. Rev. Lett.*, 2003, **91**, 185502.

